

Chapter 3

Homographically generated light-sheets

No

— James Manton

Commercial and home-built[1] light-sheet systems typically use a cylindrical lens to convert a circular Gaussian laser beam into a thin sheet, as discussed in Chapter 1. Alternatively, Digitally scanned Light-sheet Microscopy (DSLM) uses galvanometric mirrors can mimic this effect mechanically by rapidly dithering a laser beam. [2]. Using galvanometric mirror pairs enables fast sweeping of the light-sheet through a static specimen. However, the use of a scan lens can lead to registration errors of the sheet with respect to the imaging plane, leading to an excess background fluorescence in large volumes. This chapter compares nonlinear and linear methods for registering the stack excitation and imaging planes in a DSLM system. The work presented in this chapter, was submitted and accepted for publication in Optics Letters [3]

3.1 Homographic theory

3.1.1 Affine region of interest

Aligning a digitally scanned light-sheet to a detection plane requires generating a control signal (V_x, V_z) for the scanning mirrors. In two dimensions the x mirror extrema map to the edges of the imaging-FOV and a linear ramp between these coordinates produces a virtual light-sheet. The z -mirror extrema correspond to the top and bottom observed image planes. However, using linear ramping from a starting point, only three of the four $x z$ extrema can be registered [4]. The fourth point is either discarded, or more typically, only the centre of the one of the axial planes is considered, essentially averaging the third and forth available vertices. As illustrated in Fig. 3.1, this assumption then leads to a poorly-registered illumination in the plane where the fourth coordinate was neglected and greater background fluorescence in Three Dimensional (3D) imaging.

3.1.2 Projective region of interest

The stack of illumination planes used in a 3D observation can be better matched to the detection planes by registering four corners of the available excitation 3D-FOV, using a projective transform. Projective transforms can map any quadrilateral onto any other, versus an affine transformation which is limited to three points. Higher order corrections could also be used, with an n -point correction using b-splines being one, computationally expensive option. However, such elastic transforms require more correspondences and are likely to incur additional errors through correspondence localisation precision. Moreover, such fiducial marks are difficult to localise, within a single Two Dimensional (2D)-FOV there are only four sufficiently valid points i.e. the four corners of the image.

3.1.3 Homography and homogenous coordinates

A calibration experiment provides the control signals (V_{x_i}, V_{z_i}) for $i = 1$ to 4, needed to register the illumination to the four extrema of the imaging volume, (x_i, z_i) . In a projective transform of \mathbf{r} , the augmented vector $\tilde{\mathbf{r}} = (x, z, 1)$ is generated and then apply a linear transform to obtain $\tilde{\mathbf{r}}' = \mathbf{H}\tilde{\mathbf{r}}$, followed by descaling to obtain the

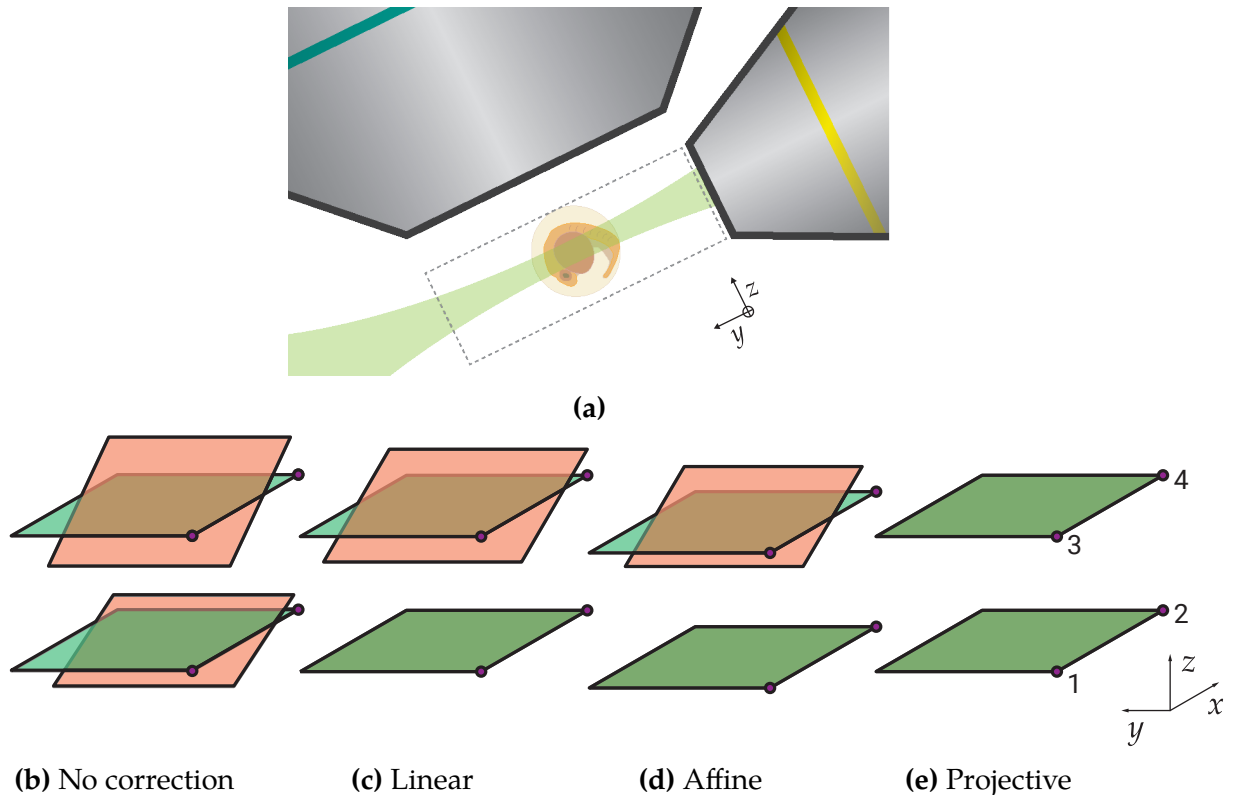


Fig. 3.1 (a) Schematic of light-sheet optics using a large NA imaging objective, the incident beam is scanned in x to create a virtual light-sheet. In b-(e) and for best image quality, the illumination planes (shown as red when not perfectly registered to the illumination planes) must be registered to the detections planes (green). The linear registration (c) tends to produce non-uniform out of focus illumination across the image. The affine registration (d) is commonly used to match the image centres between the top and bottom planes however the projective registration (e), for four control points, provides superior performance due to decreased out-of-focus fluorescence.

transformed vector

$$\mathbf{r}' = \begin{pmatrix} \tilde{r}_1' & \tilde{r}_2' \\ \tilde{r}_3' & \tilde{r}_3' \end{pmatrix}^T \quad (3.1)$$

A projective transform of a plane can be exactly defined by four projected points, unless any three are collinear. The calibration experiment identifies four (non-collinear) extrema of the imaging volume, and so it is possible to combine the augmented form of three of the positions to produce the fourth, such that

$$\lambda \begin{pmatrix} x_1 \\ z_1 \\ 1 \end{pmatrix} + \mu \begin{pmatrix} x_2 \\ z_2 \\ 1 \end{pmatrix} + \nu \begin{pmatrix} x_3 \\ z_3 \\ 1 \end{pmatrix} = \begin{pmatrix} x_4 \\ z_4 \\ 1 \end{pmatrix} \quad (3.2)$$

Where λ, μ and ν are constants. This relation can be expressed as

$$\begin{pmatrix} x_1 & x_2 & x_3 \\ z_1 & z_2 & z_3 \\ 1 & 1 & 1 \end{pmatrix} \begin{pmatrix} \lambda \\ \mu \\ \nu \end{pmatrix} = \begin{pmatrix} x_4 \\ z_4 \\ 1 \end{pmatrix} \quad (3.3)$$

After solving for λ, μ and ν the matrix \mathbf{M} can be constructed

$$\mathbf{M} = \begin{pmatrix} \lambda x_1 & \mu x_2 & \nu x_3 \\ \lambda z_1 & \mu z_2 & \nu z_3 \\ \lambda & \mu & \nu \end{pmatrix} \quad (3.4)$$

The matrix \mathbf{M} maps basis vectors to specific points, so that:

$$\mathbf{M}(100)^T \mapsto k_1(x_1, z_1, 1)^T \quad (3.5)$$

$$\mathbf{M}(010)^T \mapsto k_2(x_2, z_2, 1)^T \quad (3.6)$$

$$\mathbf{M}(001)^T \mapsto k_3(x_3, z_3, 1)^T \quad (3.7)$$

$$\mathbf{M}(111)^T \mapsto (x_4, z_4, 1)^T$$

Since \mathbf{M} maps basis vectors to augmented positions, \mathbf{M}^{-1} decomposes an augmented position into basis vectors. The calibration experiment provides control

signals (V_{x_i}, V_{z_i}) which can be transformed to augmented vectors and treated in the same way. Specifically, $\lambda'(V_{x_1}, V_{z_1}, 1) + \mu'(V_{x_2}, V_{z_2}, 1) + \nu'(V_{x_3}, V_{z_3}, 1) = (V_{x_4}, V_{z_4}, 1)$ for constants λ', μ' and ν' so:

$$\begin{pmatrix} \lambda' \\ \mu' \\ \nu' \end{pmatrix} = \begin{pmatrix} V_{x_1} & V_{x_2} & V_{x_3} \\ V_{z_1} & V_{z_2} & V_{z_3} \\ 1 & 1 & 1 \end{pmatrix}^{-1} \begin{pmatrix} V_{x_4} \\ V_{z_4} \\ 1 \end{pmatrix} \quad (3.8)$$

The matrix \mathbf{N} can be created, in the same way that \mathbf{M} was

$$\mathbf{N} = \begin{pmatrix} \lambda' x_1 & \mu' x_2 & \nu' x_3 \\ \lambda' z_1 & \mu' z_2 & \nu' z_3 \\ \lambda' & \mu' & \nu' \end{pmatrix} \quad (3.9)$$

\mathbf{N} maps from basis vectors to augmented signals, so that $\mathbf{N}(111)^T = (V_{x_4}, V_{z_4}, 1)^T$. To compute the projective transform of an illumination position $\mathbf{r} = (x, z)^T$ to the required control signal $\mathbf{V} = (V_x, V_z)^T$, we simply need to convert the augmented position to basis vectors using $\mathbf{M}^{-1}\tilde{\mathbf{r}}$, and the basis vectors to control signals using \mathbf{N} with dehomogenisation. It is useful to use the homography matrix $\mathbf{H} = \mathbf{NM}^{-1}$, so that $\tilde{\mathbf{V}} = \mathbf{H}\tilde{\mathbf{r}}$, or

$$\begin{pmatrix} \tilde{V}_x \\ \tilde{V}_z \\ k \end{pmatrix} = \begin{pmatrix} \lambda' V_{x_1} & \mu' V_{x_2} & \nu' V_{x_3} \\ \lambda' V_{z_1} & \mu' V_{z_2} & \nu' V_{z_3} \\ \lambda' & \mu' & \nu' \end{pmatrix} \begin{pmatrix} 0 & 1 & 0 \\ -z_1 & z_2 & z_3 \\ -1 & 1 & 1 \end{pmatrix}^{-1} \begin{pmatrix} x \\ z \\ 1 \end{pmatrix} \quad (3.10)$$

where the x range is normalised to run from $x_1 = x_3 = 0$ to $x_2 = x_4 = 1$, and \mathbf{M}^{-1} is heavily simplified by solving for λ, μ and ν . Finally,

$$\begin{pmatrix} V_x \\ V_z \end{pmatrix} = \frac{1}{k} \begin{pmatrix} \tilde{V}_x \\ \tilde{V}_z \end{pmatrix} \quad (3.11)$$

rescales homogeneous voltages to real output voltages. Non-extrema points can therefore be interpolated to create signal trains rather than point-wise; for higher-order corrections point-wise generation would be necessary.

3.2 Experimental implementation and verification

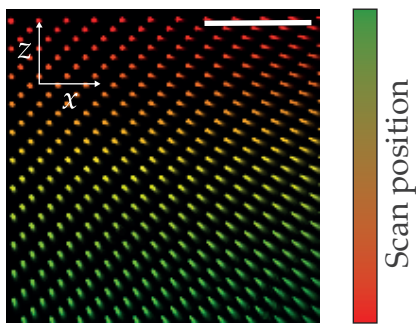
3.2.1 Scan lens characterisation

To accurately measure the deviation solely caused by the scanning system, a camera (Thorlabs DCC1545M) was mounted directly after the scan lens and an attenuated beam was imaged directly onto the sensor. The full range of the scanning unit was considered by incrementing mirror control voltages (V_x , V_z) linearly in input space, and imaging the illumination beam in xz for each step, as shown in Fig. 3.2a. Each beam profile was fit with a 2D Gaussian to create a map of xz illumination positions corresponding to constant steps in scan lens. Fig. 3.2b and 3.2c show the residual deviation from desired positions when using a 3 pt and 4 pt registration respectively. The 4 pt correction is more faithful to experimental values. The figure verifies that a 4 pt correction will produce a more valid fitting for a beam scanned across a telecentric lens, with a more significant improvement becoming apparent when using a larger region of the scan lens.

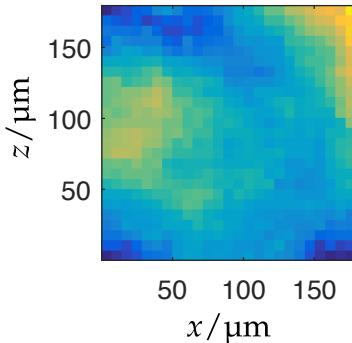
3.2.2 *in situ* characterisation

In real samples for light-sheet microscopy, a mismatch between the detection plane and the illumination plane can reduce image fidelity due to decreased illumination in the imaging plane as well as excess background fluorescence. Fig. 3.3 show the 4 pt registration largely eliminates this mismatch for real samples including fluorescent beads, dyes and a model organism.

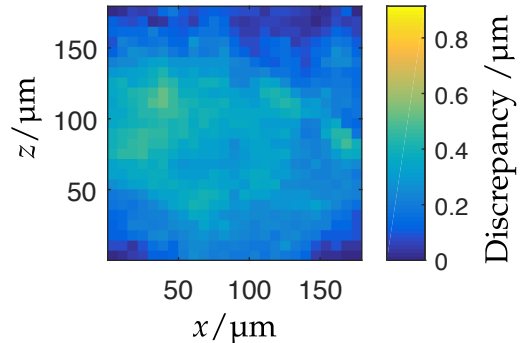
In Fig. 3.3a-3.3b Fluorescent beads (TetraSpeck 100nm Microspheres) were dispersed in 1.5% agarose at 1:1000 concentration and imaged using a 3 pt and a 4 pt registration. Each bead (of ~ 500) was localised in 3D and its peak fluorescence intensity was compared in the 4 pt and 3 pt case, and was found to be, on average, 42% higher across the entire volume ($512 \mu\text{m} \times 512 \mu\text{m} \times 100 \mu\text{m}$) for the 4 pt registration. For a $10 \mu\text{m}$ light-sheet this corresponds to an axial light-sheet mismatch of $6.9 \mu\text{m}$ on average, for the 3 pt case. The experiment from Fig. 3.2 was repeated in the light-sheet microscope using dye solution for Fig. 3.3c. The scanning beam was paused and iterated again through discrete positions in the imaging volume. Each record fluorescent dye image was characterised by a focus measure, obtained by finding the intensity maximum through the focus of the light-sheet for each beam



(a) Raw data of a point scanning across a scan lens. Scale bar is 1 mm



(b) 3 pt correction discrepancy map



(c) 4 pt correction discrepancy map

Fig. 3.2 Scan lens characterisation. Fig. (a) shows the illumination profile in the xz plane for 400 scan positions, with a 3 pt registration. The beam positions in (a) were each localised by fitting a 2D Gaussian. The identified positions using a 3 pt (b) and 4 pt (c) show that the positional discrepancy of the 3 pt method is largely fixed by the 4 pt registration.

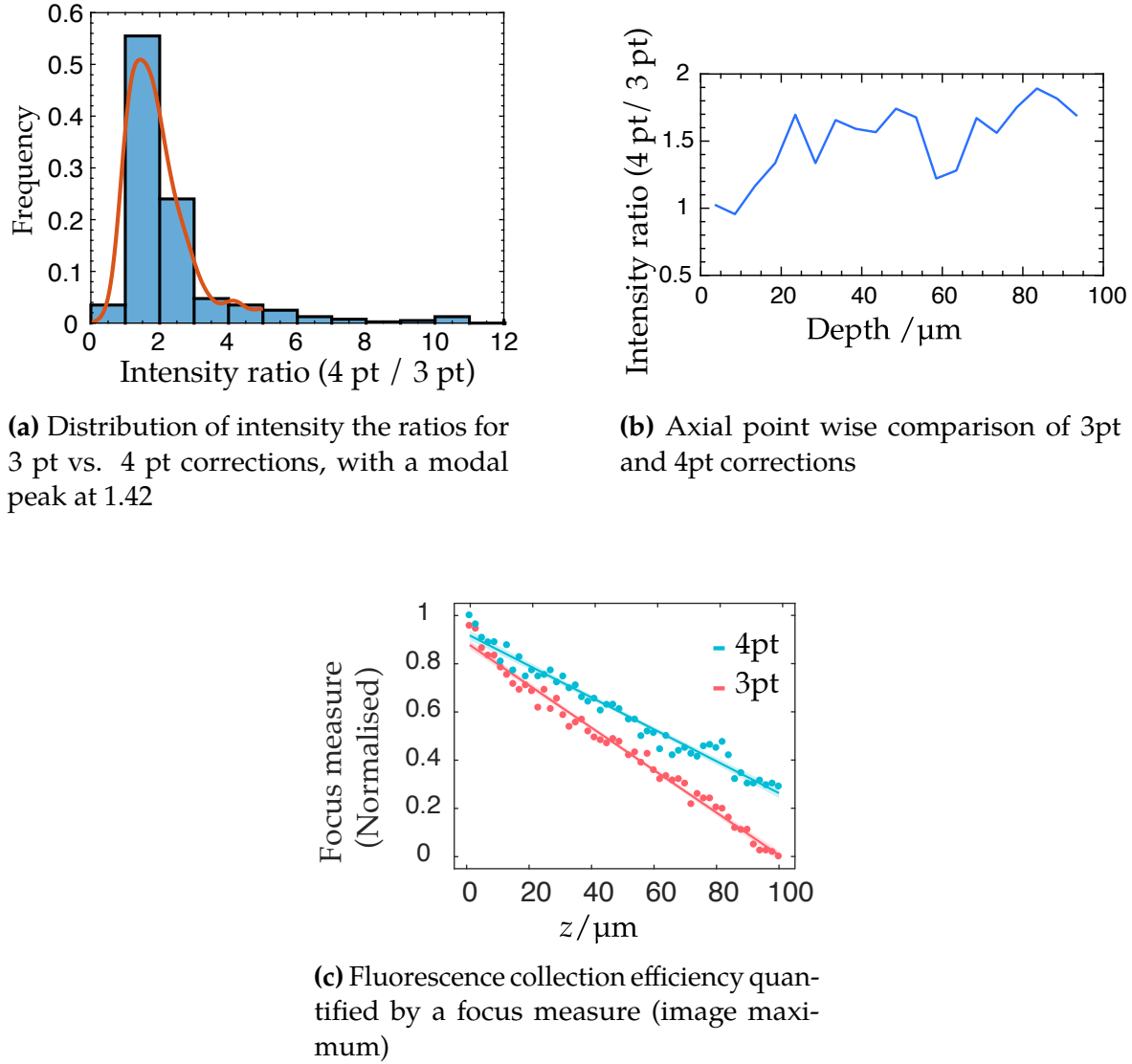


Fig. 3.3 *in situ* characterisation using beads and dye: (a-b) Ratios of intensity maxima of localised fluorescent bead images were compared in 3D observation volumes using 3 pt and 4 pt corrections. The ratios in (a) show an average 42% increase in contrast using a 4 pt. correction, with an increasing effect when traveling axially (b). (c) is the corresponding graph for a beam scanned through dye solution also demonstrates greater light capture efficiency which becomes more significant with depth. The image maxima was taken as a good measure of beam to image plane focus.

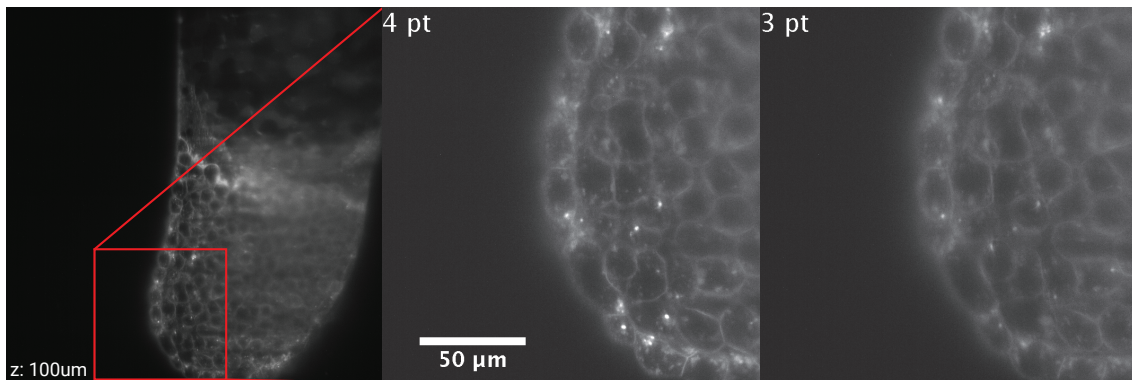


Fig. 3.4 Correction demonstrated in model organism: Presented is a transgenic Zebrafish expressing mCherry:beta-actinCAAX, in which the membrane contrast is substantially improved by the 4 pt registration.

position. As expected, greater depth degraded how well matched the beam was to the focal plane more sharply for the 3 pt correction than the 4 pt.

The advantages of using a 4 pt correction were then finally demonstrated in Zebrafish (*Danio rerio*). The sample used in Fig. 3.4 transgenically expressed mCherry near the cellular membrane (Beta-actin: mcherryCAAX) and mounted in 1.2 % agarose; the sample itself was 4 hours post-fertilisation.

3.3 Conclusions

Considerations in registration between detection and illumination volumes[5] are becoming increasingly pertinent with the current trends of exceptionally large samples[6] being imaged at diffraction limited resolution and at depth[7, 8]. Advances in cameras[9, 10], optics[11] and fast piezo technology will further exaggerate errors introduced when using linearly generated waveforms in the next generation of light-sheet microscope.

It was demonstrated that, for inverted Selective-Plane Imaging Microscope (iSPIM) systems using virtual light-sheets, a 4 pt correction (non-linear waveform generation) versus a 3 pt correction (affine waveform generation) will better counteract errors introduced by beam scanning optics, conveniently and for minimal computational cost.

The following chapter will follow on by partially applying the mathematics presented here to help better register volumes in Optical Projection Tomography (OPT) reconstructions, specifically for systems with systematic mechanical error.

References

1. Pitrone, P. G. *et al.* OpenSPIM: an open-access light-sheet microscopy platform. *Nature methods* **10**, 598–9 (2013).
2. Keller, P. J. *et al.* Fast, High-Contrast Imaging of Animal Development with Scanned Light Sheet-Based Structured-Illumination Microscopy. *Nature Methods* **7**, 637–642 (2010).
3. Russell, C. T., Rees, E. J. & Kaminski, C. F. Homographically Generated Light Sheets for the Microscopy of Large Specimens. *Optics Letters* **43**, 663–666 (2018).
4. Zitová, B. & Flusser, J. Image Registration Methods: A Survey. *Image and Vision Computing* **21**, 977–1000 (2003).
5. Royer, L. A. *et al.* Adaptive Light-Sheet Microscopy for Long-Term, High-Resolution Imaging in Living Organisms. *Nature Biotechnology* **advance online publication** (2016).
6. Chen, F., Tillberg, P. W. & Boyden, E. S. Expansion Microscopy. *Science* **347**, 543–548 (January 2015).
7. Wang, K. *et al.* Direct Wavefront Sensing for High-Resolution in Vivo Imaging in Scattering Tissue. *Nature Communications* **6**, 7276 (2015).
8. Truong, T. V., Supatto, W., Koos, D. S., Choi, J. M. & Fraser, S. E. Deep and fast live imaging with two-photon scanned light-sheet microscopy. *Nature methods* **8**, 757–60 (2011).

9. Zheng, G., Ou, X. & Yang, C. 0.5 Gigapixel Microscopy Using a Flatbed Scanner. *Biomedical Optics Express* **5**, 1–8 (2014).
10. Brady, D. J. *et al.* Multiscale Gigapixel Photography. *Nature* **486**, 386–389 (2012).
11. Sofroniew, N. J., Flickinger, D., King, J. & Svoboda, K. A Large Field of View Two-Photon Mesoscope with Subcellular Resolution for in Vivo Imaging. *eLife* **5**, e14472 (2016).